Conductivity tomography at two frequencies

Junxing Cao*, Zhenhua He*, Jieshou Zhu*, and Peter K. Fullagar‡

ABSTRACT

We present a new approach for crosshole radio tomography. Conductivity images of the investigated area are reconstructed from the ratio of the electric field intensities measured at two similar frequencies. The method largely avoids assumptions about the radiation pattern and in-situ intensity of the transmitting antenna, which introduce errors in conventional single-frequency crosshole electromagnetic-absorption tomography. Application of the method to field data achieved an improvement in resolution of anomalies over traditional single-frequency absorption tomography. The dual-frequency method is not a universal approach; it is suitable for moderately conductive media (>0.01 S/m) over the approximate frequency range 1–100 MHz.

INTRODUCTION

Electrical conductivity is one of the most important petrophysical parameters. It is very sensitive to rock porosity and degree of saturation with different types of pore fluids. Crosshole radio tomography is being applied increasingly in geophysical exploration for high-resolution delineation of electrical conductivity variations. It has found successful applications in mineral exploration (Wu and Xing, 1982; Stolarczyk, 1992; Fullagar et al., 2000), engineering and environmental investigations (Wu and Zhang, 1998), and coal mining (Vozoff et al., 1993). Crosshole radio-absorption tomography, pioneered by Lager and Lytle (1977), is an imitation of X-ray absorption tomography in medicine. However, there are some differences in physical scale and scanning geometry (Dines and Lytle, 1979), and in the predictability of source strength.

Source strength (i.e., the incident field intensity) serves as the reference for the calculation of the absorption in absorption tomography. Source strength in X-ray tomography can be treated as a constant. However, the source strength in geophysical surveys is dependent on host properties and the transmitter-receiver azimuth, and so is variable. Determination of the source strength is one of the key steps for crosshole radio-absorption tomography. However, the source strength cannot be measured directly or calculated exactly. An amplitude ratioing method for receivers at different distances, proposed by Grubb and Wait (1971), is sometimes used to eliminate the source strength (Wu and Xing, 1982). The method is only suitable for the case when there are at least three boreholes in a straight line and the rock is reasonably homogeneous. Feng et al. (1995) proposed an iterative method to estimate the source strength. It is only suitable for weakly inhomogeneous media, where the source strength can be treated as a constant. For highly inhomogeneous cases, such as in mineral exploration, there is still no way to precisely determine the source strength.

Calculation of the radiation pattern of the transmitter also poses a difficult problem. In practice, the real radiation pattern is usually approximated by the radiation pattern of a half-wavelength antenna.

Errors in the estimation of the source strength and radiation pattern often result in distortions of the reconstructed tomogram. In this paper, we present a new tomographic methodology that does not require calculation of the source strength and the radiation pattern. Conductivity images are reconstructed from the ratio of the electric field intensities measured at two frequencies. An application of the method to field data reveals an improvement in image resolution relative to traditional single-frequency absorption tomography.

THEORY

Crosshole radio surveys often use electric dipole antennas as transmitter (Tx) and receiver (Rx). For a center-fed electric dipole antenna in an unbounded homogeneous isotropic medium, the electric field intensity in the far field can be expressed as (Wu and Xing, 1982, 15; Mott, 1992, 29)

$$
\begin{aligned}
e &= \frac{\omega \mu I_0}{4\pi\alpha} \frac{e^{-\beta r}}{r} \frac{\cos[(\alpha L/2)\cos\theta] - \cos(\alpha L/2)}{\sin\theta} \cdot \cos(\varphi) \\
&= e_0 \frac{e^{-\beta r}}{r} P(\theta) \cos(\varphi),
\end{aligned} \tag{1}
$$

where $\omega = 2\pi f$ is the angular frequency of the Tx dipole; μ is the magnetic permeability of the medium; I_0 is the feeding current amplitude, assuming the current in the antenna is of the form $I = I_0 \sin[\alpha(L/2 - |z|)]e^{-j\omega_t}$; α and β are, respectively, the electromagnetic (EM) phase and absorption coefficients of the medium; r is the distance between the center points of the transmitting and the receiving antennas; L is the length of the antenna; θ is the polar angle, the angle between the transmitter axis and the ray path; φ is the angle between the Tx axis and the Rx axis ($\varphi = 0$ when Tx and Rx are parallel); e_0 is the primary radiation intensity of the transmitter (i.e. the source strength); and $P(\theta)$ is the radiation pattern of the transmitting antenna. The phase and absorption coefficients (α, β) of a homogeneous medium can be expressed as

$$\alpha = \left(\frac{\omega^2 \mu \varepsilon}{2}\right)^{1/2} \left\{\left[1 + \left(\frac{\sigma}{\omega \varepsilon}\right)^2\right]^{1/2} + 1\right\}^{1/2}, \quad (2)$$

$$\beta = \left(\frac{\omega^2 \mu \varepsilon}{2}\right)^{1/2} \left\{\left[1 + \left(\frac{\sigma}{\omega \varepsilon}\right)^2\right]^{1/2} - 1\right\}^{1/2}. \quad (3)$$

where σ and ε are the conductivity and permittivity, respectively. When $\sigma/\omega\varepsilon > 10$, the medium can be treated as a good conductor, and expressions (2) and (3) can be approximated as

$$\alpha \approx \beta \approx (\omega\mu/2)^{1/2} \cdot \sigma^{1/2}. \quad (4)$$

Fixing the Tx and Rx's orientation and position, and operating the transmitter at two similar frequencies ω_1 and ω_2, two electrical intensities e_1, e_2 will be observed. From expression (1), the ratio e_1/e_2 can be expressed as

$$\frac{e_1}{e_2} = \frac{f_1}{\alpha_1} \cdot \frac{\alpha_2}{f_2} \cdot \frac{e^{-\beta_1 r}}{e^{-\beta_2 r}} \cdot \frac{P_1(\theta)}{P_2(\theta)}. \quad (5)$$

The unit of e_1 and e_2 is volts/meter. In deriving expression (5), it is implicitly assumed that $\mu_1 = \mu_2 = \mu_0$, and that the primary field intensity $e_0 = \omega\mu_0 I_0/4\pi\alpha$ is independent of frequency over the small frequency range $\Delta f = f_2 - f_1$.

For small Δf, $P_1(\theta) \approx P_2(\theta)$, and expression (5) reduces to

$$\frac{e_1}{e_2} = \frac{f_1}{\alpha_1} \cdot \frac{\alpha_2}{f_2} \cdot e^{\beta_2 r - \beta_1 r}. \quad (6)$$

Substituting expression (4) into expression (6), we have

$$\frac{e_1}{e_2} = (f_1/f_2)^{1/2} \cdot e^{(\mu_0\pi)^{1/2}(f_2^{1/2} - f_1^{1/2})\sigma^{1/2} r}. \quad (7)$$

Taking logarithms of equation (7),

$$E_1 - E_2 = 20\log_{10}(f_1/f_2)^{1/2} + 8.6859(\pi\mu_0)^{1/2}$$
$$\times \left(f_2^{1/2} - f_1^{1/2}\right)\sigma^{1/2} r,$$

where E_1 and E_2 are in decibels.

Discretizing the interwell region into $n_x \times n_z = n$ cells, with the conductivity in each cell constant, the above equation can be written in the discrete form (see Figure 1)

$$E_1 - E_2 = 20\log(f_1/f_2)^{1/2} + 8.6859(\pi\mu_0)^{1/2}$$
$$\times \left(f_2^{1/2} - f_1^{1/2}\right) \sum_{j=1}^{n} \sigma_j^{1/2} r_j, \quad (8)$$

where r_j is the length of the ray segment in the jth cell. If the ray in question does not pass through cell j, $r_j = 0$. Equation (8) is a general expression for both the straight-ray and bent-ray cases (Figure 1). For a continuous conductive medium, the summation in equation (8) should be replaced with $\sum_{j=1}^{n} \int_{r_{in}}^{r_{out}} \sigma_j^{1/2}(r)\, dr$, and the new equation is suitable for the bent-ray case; r_{in} and r_{out} in $\int_{r_{in}}^{r_{out}} \sigma_j^{1/2}(r)\, dr$ are the entry and exit points along the ray passing through cell j, whereas $\sigma_j(r)$ is the conductivity distribution in cell j.

Equation (8) can be rewritten as

$$\sum_{k=1}^{n} \sigma_k^{1/2} r_k = b, \quad (9)$$

where

$$b = C_1 \cdot (E_1 - E_2) - C_2 \quad (9a)$$

where $C_1 = 57.944/(f_2^{1/2} - f_1^{1/2})$ and $C_2 = 20\log(f_1/f_2)^{1/2} \cdot C_1$.

Equation (9) defines a linear relation between the measured data E_1, E_2 and the discrete conductivity distribution $\sigma_k^{1/2}(k = 1, n)$. For m measured data, equation (9) can be expressed in the following matrix form:

$$\mathbf{A}_{m \times n} \mathbf{x}_n = \mathbf{b}_m, \quad (10)$$

where the element a_{ij} of $\mathbf{A}$ is the length of ray i in cell j; $\mathbf{x} = (\sigma_1^{1/2}, \sigma_2^{1/2}, \ldots, \sigma_n^{1/2})^T$ is the unknown parameter vector; and $\mathbf{b} = (b_1, b_2, \ldots, b_m)^T$ is the known data vector. Solving equation (10), we obtain the discrete conductivity distribution image. By ratioing the responses at two frequencies, dependence on the primary radiation intensity e_0 and the radiation pattern $P(\theta)$ of the transmitting antenna has been eliminated.

FIELD EXAMPLE

Site geology

The experiment site was located in the center of Chengdu City, Sichuan Province, China, on the western rim of the Sichuan basin. The bedrock in the region is composed of Cretaceous sandstones and mudstones. The overburden is loose Quaternary pebble sands and clays. The thickness of the
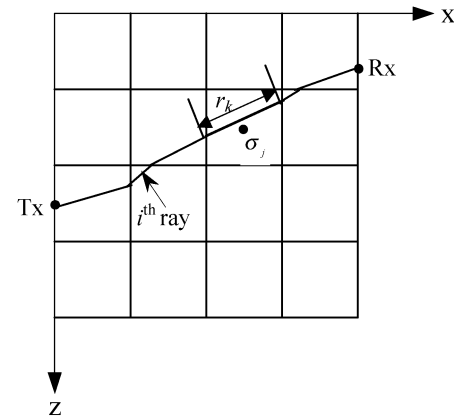

FIG. 1. Schematic showing the discretization of the image plane and a typical raypath through jth cell, where Tx denotes the transmitter and Rx denotes the receiver.

overburden is about 30 m. In routine drilling of the foundation of a large building, several fine sand layers with thickness of 0.1–1.2 m were discovered. If the thickness and extent of a fine sand layer exceeds a critical value, it may liquefy under heavy load. The main goal of the cross-borehole radio probing was to determine the extent of the fine sand layers. The uppermost 4 m of the overburden will be excavated. Therefore, our radio probing began at a depth of 4 m.

There were eight boreholes at the site. Radio surveys were performed between four pairs of boreholes. Just one tomographic panel is considered here, between the vertical boreholes YG21 and YG22, 19.2-m apart. The depth of the holes is 31 m, with both terminating about 1 m into bedrock. The geological logs of borehole YG21 and YG22 are presented, respectively, on the left side and right side of the absorption tomogram and conductivity tomogram (Figures 4 and 5, respectively). It should be pointed out that the division between the mid-dense pebble and the dense pebble in the geological logs is not always clear. The main factor that determines the propagation characteristics of radio waves in the interwell medium is underground water. The water table depth at the site is 7 m. The medium beneath the water table is of higher conductivity.

Data acquisition

The data were recorded with a JW-4 electric dipole system in May 1996. The JW-4 is a crosshole radio-frequency EM system (Qu et al., 1991; Fullagar et al., 1996), developed by the Chinese Institute of Geophysical and Geochemical Exploration (IGGE). The transmitter is notionally a half-wave electric dipole, with antenna arms extending up to 18 m on either side of the electronics pod, depending on the operating frequency. The transmitter used in our survey was a dipole antenna with two 1-m arms. The receiver antenna was a 1-m monopole. Electric field intensities were recorded at 11 frequencies between 12 and 32 MHz with an interval of 2 MHz. Data were recorded as common-transmitter gathers, recorded with the transmitter at a fixed position in one well while the receiver scanned along the other borehole. The sampling interval along the borehole for the transmitter was 1.0 m; that for the receiver was 0.5 m. Reciprocal measurements were recorded, with the positions of transmitter and receiver reversed.

Before the tomographic measurements, a horizontal synchronization ("parallel scan") survey was performed. Horizontal synchronization means the transmitter and the receiver are located at same level and are moved down or up at the same speed. The sampling interval along the borehole in the horizontal synchronization survey was 1.0 m for both the transmitter and the receiver. The horizontal synchronization data are ordinarily used to estimate the background 1D conductivity structure of the inspected profile and to determine suitable operating frequencies. Horizontal-ray electric-field intensities measured at a range of frequencies between boreholes YG21 and YG22 are shown in Figure 2. Intensity of −140 dB means no valid signal is received. The curves show that the measured field intensities are dependent on the operating frequency.

Conductivity tomography at two frequencies

Conductivity tomography at two frequencies involves the following steps:

Choose raypath style for characterization of the radio propagation.—Straight raypaths were assumed in this study. A straight-ray approximation has been commonly adopted for radio tomography. The validity of the approximation was discussed in depth by Dines and Lytle (1979) and has been tested in practice (Dines and Lytle, 1979; Cao et al., 1995; Zhou et al.,1998; Fullagar, et al., 2000).

Construct the discretised conductivity model.—The imaging plane was discreted into $19 \times 54 = 1026$ rectangle cells. The square root of conductivity within each rectangular cell was interpolated according to

$$\sigma_j^{1/2}(\xi, \varsigma) = N_1 \sigma_1^{1/2} + N_2 \sigma_2^{1/2} + N_3 \sigma_3^{1/2} + N_4 \sigma_4^{1/2},$$
(11a)

where $\sigma_j^{1/2}(\xi, \varsigma)$ is the square-root conductivity distribution in cell j; ξ, ς, are local coordinate variables; and $\sigma_1^{1/2}, \sigma_2^{1/2}, \sigma_3^{1/2}, \sigma_4^{1/2}$ denote the square-root conductivity at the four corners of the jth cell (Figure 3). N_1, N_2, N_3, N_4, are the interpolation base functions, given by

$$N_1 = \frac{(\ell - \xi)(h - \zeta)}{\ell h},$$
$$N_2 = \frac{\xi(h - \zeta)}{\ell h},$$
$$N_3 = \frac{\xi \cdot \zeta}{\ell h},$$
$$N_4 = \frac{(\ell - \xi)\zeta}{\ell h}.$$
(11b)

where ℓ is the horizontal side length of the cell and h is the vertical side length (Figure 3). For the example considered here, $\ell = 1.01$ m, $h = 0.5$ m. The discrete model is a piecewise continuous approximation of the actual conductivity. In the discrete model, the unknown parameters were the square-root conductivities at the grid nodes. The number of the unknowns
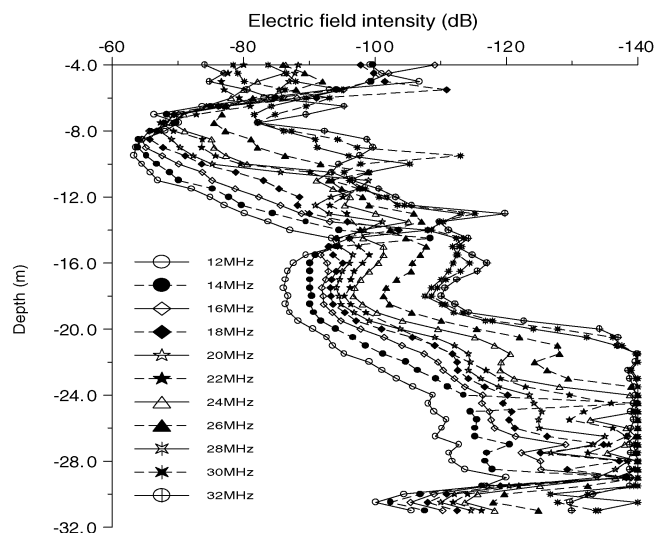

FIG. 2. Plot showing the horizontal-ray electric-field intensities measured between YG21 and YG22. The curves show the dependence on frequency of the electrical field intensities. Intensity of –140 dB means no valid signal is received. Surface is at depth z = 0 m.

$(20 \times 55 = 1100)$ was therefore larger than the number of the cells.

Generate the coefficient matrix for the tomographic equations.—For ray i, from the Tx to the Rx, find all the cells which it traverses. For each such cell, integrate the interpolation functions along the (straight) ray segment to compute the following coefficients:

$$C_{u,v}^{(1)} = \frac{1}{\ell h} \int_{\xi_{in}}^{\xi_{out}} (\ell - \xi)(h - \zeta) \, d\xi,$$

$$c_{u,v+1}^{(2)} = \frac{1}{\ell h} \int_{\xi_{in}}^{\xi_{out}} \xi(h - \zeta) \, d\xi,$$

$$C_{u+1,v+1}^{(3)} = \frac{1}{\ell h} \int_{\xi_{in}}^{\xi_{out}} \xi \cdot \zeta \, d\xi,$$

$$C_{u+1,v}^{(4)} = \frac{1}{\ell h} \int_{\xi_{in}}^{\xi_{out}} (\ell - \xi) \cdot \zeta \, d\xi,$$

$$\zeta = \frac{\zeta_{in} - \zeta_{out}}{\xi_{in} - \xi_{out}} \xi + \zeta_{in}, \tag{12}$$

where $c_{u,v}, c_{u,v+1}, c_{u+1,v}, c_{u+1,v+1}$ are the components of the coefficient matrix elements; subscript u, v etc. are the global serial number of the relevant unknowns in the whole discrete grid; and superscripts $1, 2, 3, 4$ refer to the nodes of cell j. Element $a_{i,j}$ of the coefficient matrix relates to $c_{u,v}$ with $j = (u - 1) \times n_x + v$, where $n_x = 20$ is the number of nodes in the horizontal direction. After each ray-tracing calculation, those coefficients corresponding to the same node (i.e., with same global serial number) must be stacked up.

Choose the data sets to be imaged.—Data at 18 and 20 MHz were adopted as E_1 and E_2, respectively, for tomographic inversion. The known data points [i.e., the $\mathbf{b}_m$ in equation (10)] were computed using equation (9a). The total number of the known data points is 969.

Solve the tomographic equations.—The tomographic equations (10) were solved using an algebraic iterative reconstruction technique (van der Sluis and van der Vorst, 1987; Cao and
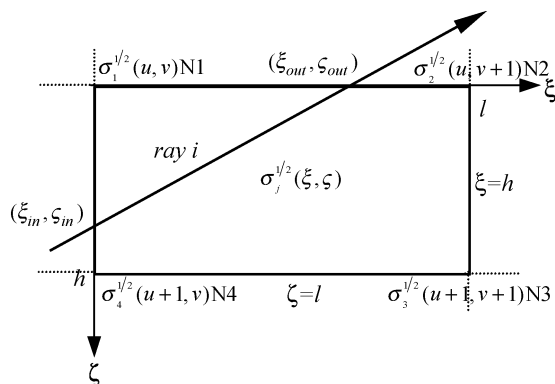
Nie, 1998), yielding the discrete conductivity distribution between borehole YG21 and borehole YG22. A homogeneous model of constant conductivity 0.1 S/m was selected as the starting model in the iterative reconstruction.

Create and interpret the tomogram.—The conductivity tomogram is shown in Figure 4. The inversion result obtained by solving equation (10) was the discrete distribution of the SQRT conductivity, then converting to conductivity. To judge the reliability of the tomogram, the geological logs are included, based on drilling and coring results. For comparison, a conductivity tomogram constructed using single-frequency (20-MHz) absorption tomography is shown in Figure 5. Significant differences are apparent between the two tomograms. The most remarkable difference is that the dual-frequency tomogram (Figure 4) shows a low-conductivity layer (blue) at approximately 4–7 m depth, whereas the increase of conductivity with depth is much more gradual in the single-frequency tomogram (Figure 5). The base of the low-conductivity layer in Figure 4 is consistent with the location of the water table. The low conductivity is associated with the dry, loose clay-grit layer. It is expected that the layers containing finer particles should have high conductivity and high absorption properties; thus, high conductivity may indicate fine sand in this region. Both tomograms reveal high-conductivity anomalies at depths
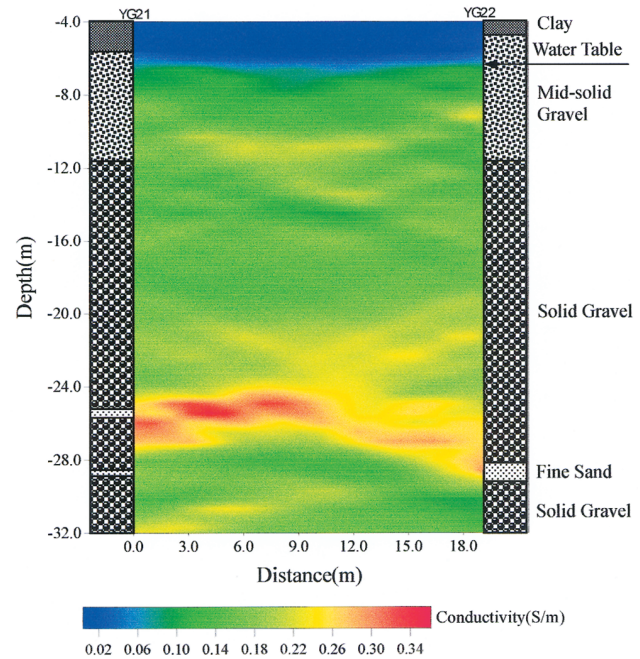

FIG. 4. Conductivity tomogram constructed using the ratio of electric field intensity at two frequencies (18 and 20 MHz). The geological logs beside the tomogram are used to evaluate the tomogram, and are based on drilling and coring results. The division between the mid-solid gravel and the solid gravel is not always clear. The tomogram shows distinctly that the medium between borehole YG21 and borehole YG22 is inhomogeneous. The low conductivity abnormality (blue area) at shallow depth (4–7 m) is the response of the dry loose clay and grit layer, and its base coincides with the water table. The high-conductivity abnormalities (red areas) at depth 24–31 m indicates the existence of fine sand layers or a high-rate fine sand and clay composing.

FIG. 3. Schematic showing the calculation of the elements, relating to cell j, of the coefficient matrix of the tomography equation. The subscript u, v in brackets are the global indices of the discrete conductivity nodes, and the subscripts 1,2,3,4 are the local serial numbers of the discrete conductivity parameters and the interpolation base functions in cell j.

of 24 to 31 m (orange-red areas). However, the extents of the high-conductivity anomalies at the boreholes are not enirely consistent with the known fine-sand layers at depth. The disagreement may arise partly from the limited resolution and partly from an offset between the lithology boundary and the electrical boundary.

Which tomogram provides the best representation of the real conductivity? We favor the dual-frequency conductivity tomogram (Figure 4). This tomogram images the base of the dry clay and grit layer at the water table exactly. The gradual transition (5–10 m depth) to higher conductivity in the 20-MHz tomogram (Figure 5) is presumed to be an artefact, perhaps arising from the assumption of a perfect half-wavelength dipole radiation pattern. The influence of the ground surface on the field intensity is arguably more severe for the single-frequency tomography.

APPLICABILITY

Operating frequency

To construct the conductivity image using the method proposed in the previous section, the following conditions must be met:

1) $\sigma/\omega\varepsilon > 50$, i.e., the medium can be treated as a good conductor and displacement currents can be neglected. (This is a fairly severe condition: $\sigma/\omega\varepsilon > 10$ would introduce only 1% error in the wave coefficients.)

2) The conductivity σ of the medium is essentially independent of frequency over the frequency range of the measurements.
3) The absorption coefficient β is frequency dependent.
4) Altering the frequency results in only a small change in the radiation pattern $P(\theta)$ (to make the problem linear with respect to $\sigma^{1/2}$). In other words, radiation pattern is assumed independent of frequency over the range in question.

All four conditions can be satisfied by an appropriate choice of the operating frequencies. Condition (1) results in the following basic principle for the choice of the frequency:

$$f < \frac{\sigma}{100\pi\varepsilon}. \tag{13}$$

Although Johnscher (1977) and others have suggested that conductivity is approximately proportional to frequency over a wide frequency range, condition (2) can be assumed for small frequency perturbations and typical earth medium. However, equations (3), (2), and (1) show that conditions (3) and (4) are somewhat conflicting [i.e., if β depends on frequency, then so will $P(\theta)$]. Equation (3) shows that the absorption coefficient β is a function of the frequency f, the electrical conductivity σ, the dielectric permittivity ε, and the magnetic permeability μ of the medium. In the diffusive (high-conductivity) case, β is almost independent of the dielectric permittivity ε, according to equation (4). For a typical earth medium, the variation in ε and μ is very limited, so that f and σ are the main factors that determine β. Figure 6 shows the relationship between the absorption β and the operating frequency f and conductivity σ in a homogeneous medium with relative permeability $\mu_r = 1$ and relative permittivity $\varepsilon_r = 15$. The absorption coefficient is strongly dependent on the operating frequency only at moderate frequencies (1–100 MHz) and relatively high conductivity (>0.01 S/m). These are the conditions under which dual-frequency conductivity tomography is viable.
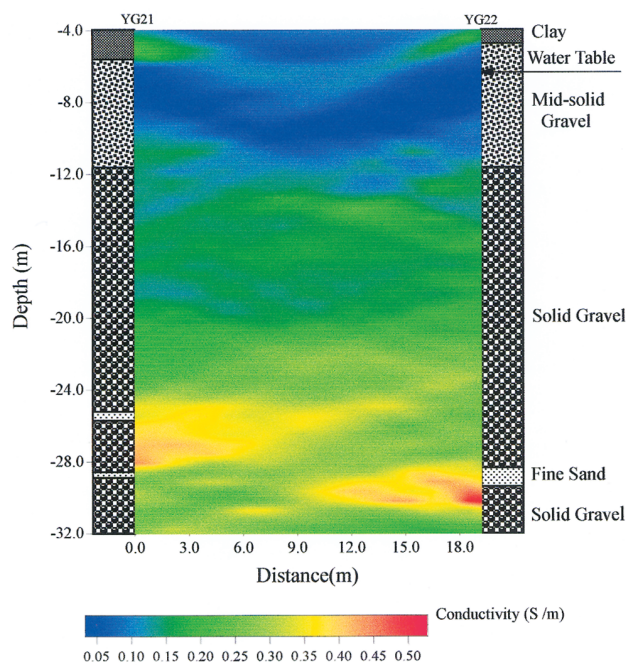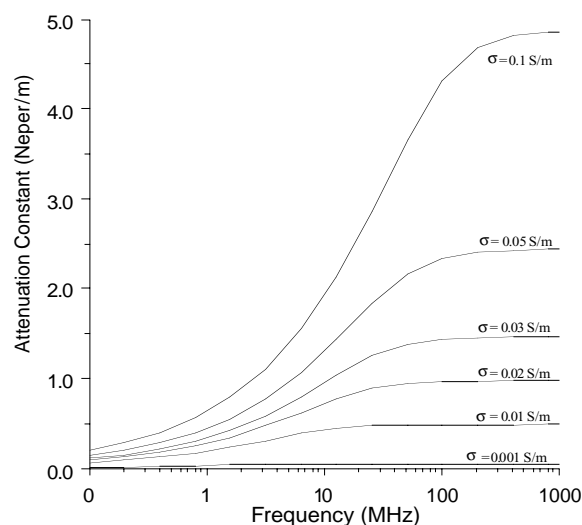

FIG. 5. Conductivity tomogram reconstructed using single-frequency absorption-tomography (20-MHz) data. The tomogram shows a general increase in conductivity with depth and the existence of conductivity abnormalities (blue and red areas). The low-conductivity belt (blue area) at 5–10 m depth is an artificial abnormality may rising from the calculation error in the radiation pattern. The geological logs beside the tomogram are same as in Figure 4.

FIG. 6. Relationship between absorption coefficient, operating frequency, and the conductivity of a homogeneous medium. In all six cases, μ_r and ε_r of the medium are 1 and 15, respectively.

Frequency difference

Under the constraint of $\sigma/\omega\varepsilon > 50$, it follows from equation (4) that

$$\frac{d\beta}{df} = \frac{d\alpha}{df} = \frac{(\pi\mu_0\sigma)^{1/2}}{2f^{1/2}} \approx 0.99 \times \left(\frac{\sigma}{f}\right)^{1/2}. \quad (14)$$

Differentiating the radiation pattern $P(\theta)$ with respect to frequency gives

$$\frac{dP(\theta)}{df} = \frac{dP(\theta)}{d\alpha}\frac{d\alpha}{df} \approx 0.495 \times \frac{l}{\sin\theta}$$
$$\times \left[\sin\left(\frac{\alpha L}{2}\right) - \sin\left(\frac{\alpha L}{2}\cos\theta\right)\cdot\cos\theta\right]\cdot\left(\frac{\sigma}{f}\right)^{1/2}, \quad (15)$$

with f in megahertz.

To obtain a reliable conductivity image, the change in absorption coefficient, denoted by $\Delta\beta$, should be greater than some lower bound, say c_d (neper/MHz). The difference between the two measurement frequencies should then satisfy the following inequality, deduced from equation (14):

$$\Delta f > \Delta f_L = c_d \cdot \left(\frac{f}{\sigma}\right)^{1/2}, \quad (16)$$

where Δf_L is the lower bound for the frequency difference.

Let $e_P = 1 - P_2(\theta)/P_1(\theta)$ be the allowable maximum error arising from the assumption $P_2(\theta) = P_1(\theta)$. We can then derive an upper bound on Δf, namely Δf_H, given by

$$\Delta f < \Delta f_H = \frac{e_P P(\theta)}{dP(\theta)/df}, \quad (17)$$

with the derivative defined in equation (15).

The upper and lower bounds of the frequency difference depend on many factors, including the conductivity σ of the medium, the base frequency f, the transmitter antenna length L, the polar angle θ, and the allowable error e_p. Conductivity is the principal factor that determines the choice of frequency difference. Figure 7 shows the dependence of the upper and lower bounds Δf_L and Δf_H on the conductivity σ for a half-wavelength antenna when $c_d = 0.01$ neper/MHz, $e_P = 0.05$, and $\theta = 60°$. The polar angle $\theta = 60°$ is at the extreme of the normal angular range for crosshole EM surveys, because data are normally collected in a fan of $60° < \theta < 120°$. The values $c_d = 0.01$ and $e_P = 0.05$ are typical for these parameters. Figure 7 shows that the maximum allowable frequency difference Δf_H decreases as conductivity increases.

Equations (16) and (17) specify the theoretically acceptable range for the frequency difference. A big frequency difference will usually produce large changes in the electric field, and hence improve the signal-to-noise ratio. However, a larger frequency difference increases the error arising from the approximation of $P_{f1}(\theta)/P_{f2}(\theta) \approx 1$. It has been shown that $P_f(60° < \theta < 120°)$ and $P_{f+\Delta f}(60° < \theta < 120°)$ exhibit a similar trend in behavior over a relatively large frequency-difference range Δf (Cao et al., 1998). Thus, $P_{f1}(\theta)/P_{f2}(\theta)$ may be almost constant in the polar angle range of interest. On this basis, it is possible in practice to use a frequency difference greater than the theoretical Δf_H. The frequency difference used in the field

example above is 2 MHz, whereas the theoretical Δf_H is about 0.5 MHz (Figure 7).

Susceptibility to noise

Generally speaking, the susceptibility of the method to noise arises in two ways. One is the susceptibility of the data to measurement error and ambient noise, and the other is the susceptibility of the tomographic algorithm (mostly the algorithms used to solve the ill-posed matrix equation) to the data errors. Susceptibility of the tomographic algorithms to data errors has been discussed by various authors (van der Sluis and van der Vorst, 1987; Cao and Nie, 1998) and will not be pursued in this paper. The ambient noise for borehole electrical field intensity measurements in our survey is of order 10^{-7} V/m or -140 dB, and so it can be neglected in many cases. The measurement error of the JW-4 borehole EM system is about 3 dB. Let e_m be the measurement error (in decibels). Then, if d_e denotes the exact data, the observed data can be expressed as $d_e \pm e_m$, and the signal-to-noise ratio of the data is d_e/e_m. For the tomography method proposed in this paper, the residual data d_{2f} can be expressed as

$$d_{2f} = d_{f1} - d_{f2} = (d_{e1} \pm e_{m1}) - (d_{e2} \pm e_{m2})$$
$$= (d_{e1} - d_{e2}) \pm (e_{m1} \mp e_{m2}),$$

where d_{f1} and d_{f2} are the recorded data at frequencies f_1 and f_2, respectively; d_{e1} and d_{e2} are the corresponding exact data; and e_{m1} and e_{m2} are the corresponding measurement errors. The above equation shows that the residual data d_{2f} can also be expressed as the sum of the exact data $(d_{e1} - d_{e2})$ and the measurement error $(e_{m1} \mp e_{m2})$. Thus, the signal-to-noise ratio of the data d_{2f} can be expressed as $(d_{e1} - d_{e2})/(e_{m1} \pm e_{m2})$. The original exact data d_{f1} and d_{f2} are often on the order of
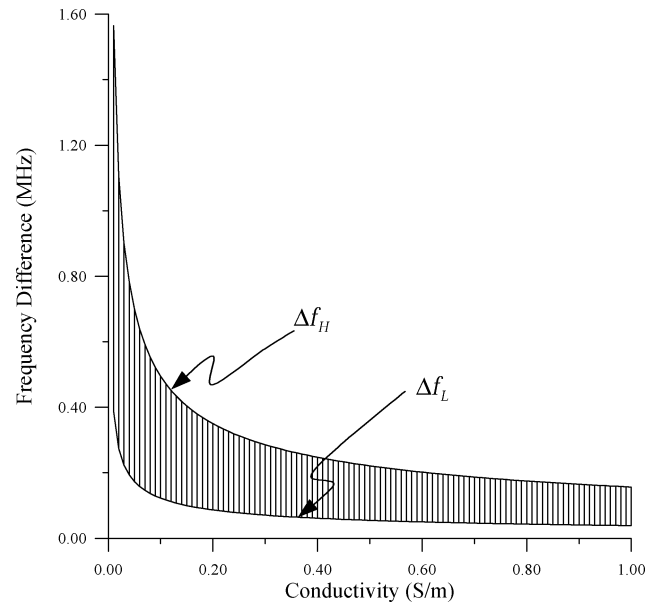

FIG. 7. Dependence on the conductivity of the medium of upper and lower bounds Δf_L and Δf_H of the frequency difference when $L = \lambda/2$, $f = 15$ MHz, $\mu_r = 1$, $c_d = 0.01$, $e_p = 0.05$, and $\theta = 60°$.

$n \times 10$ to $n \times 140$ dB ($n = 1, 2, \ldots, 9$), and the induced data d_{2f} is on the order of $n \approx 10$ (Figure 3). Generally speaking, the measurement error is a realization of a random variable with standard deviation of approximately 6 dB ($e_{m1} + e_{m2}$). Thus, the signal-to-noise ratio in the dual-frequency method will be degraded relative to that for the single-frequency absorption tomography approach owing to lower signal and higher noise.

CONCLUSION

A dual-frequency conductivity tomography approach for crosshole radio surveys has been described in this paper. Conductivity images of the investigated area are constructed from the ratio of the electric field intensities measured at two frequencies. The approach largely circumvents assumptions about the radiation pattern and in-situ radiation intensity of the transmitting antenna, which often introduce errors into single-frequency electromagnetic-absorption tomography. Application to real data shows that the proposed methodology generates a higher resolution tomogram than conventional single-frequency absorption tomography.

The method is not a universal approach. It is most suitable for relatively conductive media (>0.01 S/m) and for the frequency range of 1 to 100 MHz. Under these conditions, the dual frequency tomography approach is a valid alternative to conventional single-frequency tomography.

ACKNOWLEDGMENTS

REFERENCES

Cao, J., and Nie, Z., 1998, Model-based evaluation method for the imaging inversion algorithm and SASART algorithm: J. Chengdu Univ. of Technology, **25**, 473–479 (in Chinese with English abstract).

Cao, J., Nie, Z., and Zhu, J., 1998, Dual frequency conductivity tomography: 4th Internat. Symp., Soc. Expl. Geophys. Japan, Proc., 227–230.

Cao, J., Zhu, J., and Yan, Z., 1995, Fracture imaging using electromagnetic crosswell tomography: Proc. 3rd Soc. Expl. Geophys. Japan/Soc. Expl. Geophys. Internat. Symp. Geomography–Fracture Imaging, 220–287.

Dines, K. A., and Lytle, R. J., 1979, Computerized geophysical tomography: Proc. IEEE, **67**, 1065–1073.

Feng, R., Zhou, H., Tao, Y., and Zhang, J., 1995, Application of electromagnetic tomography in fractured zones prospecting: Proc. 3rd Soc. Expl. Geophys. Japan Internat. Symp. Geomography–Fracture Imaging, 228–235.

Fullagar, P. K., Livelybrooks, D., Zhang, P., Calvert, A. J., and Wu, Y., 2000, Radio tomography and borehole radar delineation of the McConnell nickel sulfide deposit, Sudbury, Ontario, Canada: Geophysics, **65**, 1920–1930.

Fullagar, P. K., Zhang, P., Wu, Y., and Bertrand, M.-J., 1996, Application of radio frequency tomography to delineation of nickel sulphide deposits in the Sudbury basin: SEG Intl. Exposition and 66th Ann. Internat. Mtg., Soc. Expl. Geophys., Expanded Abstracts, 2065–2068.

Grubb, R. N., and Wait, J. R., 1971, In situ measurements of the complex propagation constant in rocks from 1 to 10 MHz: Electron. Lett., **7**, 506–507.

Johnscher, A. K., 1977, The "universal" dielectric response: Nature, **267**, 673–679.

Lager, D. L., and Lytle, R. J., 1977, Determining a subsurface electromagnetic profile from high-frequency measurements by applying reconstruction techniques algorithms: Radio Sci., **12**, 249–260.

Mott, H., 1992, Antennas for radar and communications: A polarimetric approach: John Wiley & Sons, Inc.

Qu, X., Gao, W., and Zhou, H., 1991, JW-4 subsurface electromagnetic meter: Presented at Conf. on Appl. of Computing Tech. in Geosci.

Stolarczyk, L. G., 1992, Definition imaging of an orebody with the radio imaging method (RIM): IEEE Trans. Indust. Applic., **28**, 1141–1147.

van der Sluis, A., and van der Vorst, H. A., 1987, Numerical solution of large sparse linear algebraic systems arising from tomographic problems, *in* Nonet. G, Ed., Seismic tomography: D. Reidel Publishing Co., 57–87.

Vozoff, K., Smith, G. H., Hatherly, P. J., and Thomson, S., 1993, An overview of the radio imaging method in Australian coal mining: First Break, **10**, January 13–21.

Wu, Y., and Xing, F., Eds., 1982, Borehole Electromagnetic method: Geological Press (in Chinese).

Wu, Y., and Zhang, Z., 1998, A case history of protecting environment using cross-hole EM method, Proc. 4th Soc. Expl. Geophys. Japan Internat. Symp. Fracture Imaging, 411–416.

Zhou, B., Fullagar, P. K., and Fallon, G. N., 1998, Radio frequency tomography trial at Mt. Isa : Expl. Geophys, **29**, 675–679.